Mineral Carbonation of CO_2 in Mafic Plutonic Rocks, II—Laboratory Experiments on Early-Phase Supercritical CO_2-Brine-Rock Interactions

Patrícia Moita [1,2], **Edgar Berrezueta** [3], **Halidi Abdoulghafour** [4], **Massimo Beltrame** [2], **Jorge Pedro** [1,4], **José Mirão** [1,2], **Catarina Miguel** [2], **Cristina Galacho** [2,5], **Fabio Sitzia** [2], **Pedro Barrulas** [2] and **Júlio Carneiro** [1,4,*]

1   Departamento de Geociências, Escola de Ciências e Tecnologia, Universidade de Évora, Rua Romão Ramalho 59, 7000-671 Évora, Portugal; pmoita@uevora.pt (P.M.); jpedro@uevora.pt (J.P.); jmirao@uevora.pt (J.M.)
2   Laboratório HERCULES, Universidade de Évora, Largo Marquês de Marialva 8, 7000-809 Évora, Portugal; massimo@uevora.pt (M.B.); cpm@uevora.pt (C.M.); pcg@uevora.pt (C.G.); fsitzia@uevora.pt (F.S.); pbarrulas@uevora.pt (P.B.)
3   Instituto Geológico y Minero de España, C/Matemático Pedrayes 25, 33005 Oviedo, Spain; e.berrezueta@igme.es
4   Instituto de Ciências da Terra, Universidade de Évora, Rua Romão Ramalho 59, 7000-671 Évora, Portugal; halidi@uevora.pt
5   Departamento de Química, Escola de Ciências e Tecnologia, Universidade de Évora, Rua Romão Ramalho 59, 7000-671 Évora, Portugal
*   Correspondence: jcarneiro@uevora.pt; Tel.: + 351-912-857-538

check for updates

Abstract: The potential for mineral carbonation of CO_2 in plutonic mafic rocks is addressed through a set of laboratory experiments on cumulate gabbro and gabbro-diorite specimens from the Sines Massif (Portugal). The experiments were conducted in an autoclave, for a maximum of 64 days, using a CO_2 supersaturated brine under pressure and temperature conditions similar to those expected around an injection well during early-phase CO_2 injection. Multiple techniques for mineralogical and geochemical characterization were applied ante- and post-carbonation experiments. New mineralogical phases (smectite, halite and gypsum), roughness increase and material loss were observed after exposure to the CO_2 supersaturated brine. The chemical analysis shows consistent changes in the brine and rock specimens: (i) increases in iron (Fe) and magnesium (Mg) in the aqueous phase and decreases in Fe_2O_3 and MgO in the specimens; (ii) a decrease in aqueous calcium (Ca) and an increase in CaO in the cumulate gabbro, whereas in the gabbro-diorite aqueous Ca increased and afterwards remained constant, whereas CaO decreased. The geochemical model using the CrunchFlow code was able to reproduce the experimental observations and simulate the chemical behavior for longer times. Overall, the study indicates that the early-stage CO_2 injection conditions adopted induce mainly a dissolution phase with mineralogical/textural readjustments on the external area of the samples studied.

Keywords: CO_2 storage; supercritical CO_2; mafic plutonic rocks; experimental test

1. Introduction

The International Energy Agency, in its flagship report "Energy Technology Perspectives", has demonstrated that CO_2 capture, utilization and storage (CCUS) is a key technology for CO_2 emissions reduction, essential to achieve the targets set in the Paris Agreement [1].

In the CCUS chain of technologies, CO_2 is captured in large stationary sources and transported to a utilization or permanent storage in deep geological formations [2,3]. Adequate geological environments for CO_2 storage are provided by depleted hydrocarbon reservoirs, uneconomic coal seams, deep saline aquifers or mafic and ultramafic rocks [4–8]. The latter relies on the effectiveness of mineral carbonation, in which the CO_2 reacts with the enriched calcium (Ca), magnesium (Mg) and iron (Fe) minerals, to precipitate as carbonate minerals, thus ensuring safe and permanent sequestration of the CO_2 in solid phases.

Most subsurface carbon storage projects to date have injected CO_2 into sedimentary formations, either deep saline aquifers or hydrocarbon fields, but the exciting results obtained at two pilot sites where CO_2 is injected in basalts, the Carbfix and Wallula projects [9,10], have raised the profile of mafic and ultramafic rocks as suitable candidates for in situ mineral carbonation.

Although at a less developed research stage than other CO_2 storage environments, the possibility of using mafic and ultramafic rock massifs should be considered when they occur near major CO_2 emission sources. That is the case of the main industrial clusters in Sines and Setúbal. As described in an accompanying article [11], mafic and ultramafic rock massifs in southern Portugal may present a valid alternative for mineral carbonation (be it in situ, ex situ, or even enhanced weathering) of CO_2 captured in that cluster. The interested reader is directed to that paper for details on the rationale for selecting the rock massifs and their characterization.

CO_2–brine–rock interaction experiments are a well-established method to understand and explore the mechanisms and processes of geological storage [12,13]. However, unlike most previous experiments, this article focuses on mafic plutonic rocks. These have seldom been considered for in situ mineral carbonation, given the low porosity and permeability, but previous experiments on ex situ or enhanced weathering applications have been published (e.g., [14,15]).

This study deals with mineral carbonation experiments, in the laboratory, to assess the rate of reaction between CO_2 and rock samples from the Sines Massif, a subvolcanic massif mainly composed of gabbros, diorites and subordinated syenites. The laboratory experiments were designed to replicate the early stages of interaction between the mineral phases and a brine supersaturated in CO_2, as one would expect around an injection well. Indeed, we attempted to understand the initial dissolution of the rock minerals that should provide the cations to react with the dissolved CO_2.

The possible mineralogical-textural changes of the rock after interaction with brine-CO_2 was studied by a multi-analytical approach (optical microscopy (OM); scanning electron microscopy with X-ray detector (SEM-EDS); X-ray diffraction (XRD); and infrared Fourier transform spectroscopy (FTIR)) and the chemical compositional evolution of the brine and whole rock by comparative analyses (inductively coupled plasma optical emission spectrometry (ICPM-OES) and X-ray fluorescence (XRF)) before and after the experiment. Finally, numerical geochemical computation (CrunchFlow code) was used to interpret, replicate and predict the system's behavior for periods of time longer than 64 days, the maximum duration of the experiments.

The article is organized as follows: a brief background on mineral carbonation experiments and tests is presented, followed by a description of the methodology applied to characterize the rock samples and conduct the laboratory experiments. The results are then interpreted and discussed in terms of the chemical and mineral changes observed in the brine and rock surface, and according to a numerical model that reproduces the laboratory experiments and extrapolates them to longer times.

2. Background on Mineral Carbonation Experiments and Tests

During mineral carbonation, the conversion of CO_2 to stable minerals starts with the CO_2 dissolution in the aqueous phase, a function of the fluid ionic strength, pressure and temperature [16]. The resulting carbonic acid (H_2CO_3) decomposition releases hydrogen protons (H^+), lowering the pH (Equation (1)). Subsequent consumption of the H^+ due to reaction with the Mg-Ca-Fe-rich minerals

releases the metallic cations and increases the pH of the solution (Equations (2) to (6)). At suitable pH and saturation conditions, cations combine with hydrogen carbonate and form (Ca, Mg, Fe) CO_3.

$$CO_2 \text{ (g)} + H_2O \text{ (aq)} = H_2CO_3 \text{ (aq)} = H^+ \text{ (aq)} + HCO_3 \text{ (aq)} \tag{1}$$

$$\text{(Forsterite) } Mg_2SiO_4 \text{ (s)} + 4H^+ \text{ (aq)} = 2Mg^{2+} \text{ (aq)} + SiO_2\text{(aq)} + 2H_2O \text{ (l)} \tag{2}$$

$$\text{(Ca-plagioclase) } CaAl_2Si_2O_8 \text{ (s)} + 8H^+\text{(aq)} = Ca^{2+} \text{ (aq)} + 2Al^{3+} \text{ (aq)} + 2SiO_2\text{(aq)} + 4H_2O \text{ (l)} \tag{3}$$

$$\text{(Clinopyroxene) } CaMgSi_2O_6 \text{ (s)} + 4H^+ \text{ (aq)} = Ca^{2+} \text{ (aq)} + Mg^{2+} \text{ (aq)} + 2SiO_2\text{(aq)} + 2H_2O \text{ (l)} \tag{4}$$

$$Mg^{2+} \text{ (aq)} + HCO_3^- \text{ (aq)} = MgCO_3 \text{ (s)} + H^+ \text{ (aq)} \tag{5}$$

$$Mg^{2+} \text{ (aq)} + Ca^{2+} \text{ (aq)} + 2HCO_3^- \text{ (aq)} = \text{(Ca,Mg)}CO_3 \text{ (s)} + 2H^+ \text{ (aq)} \tag{6}$$
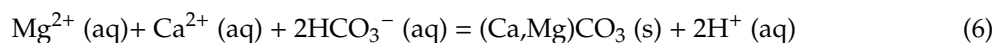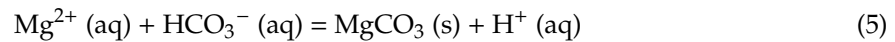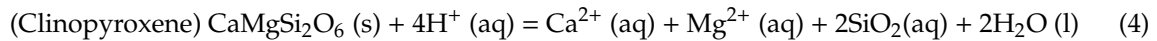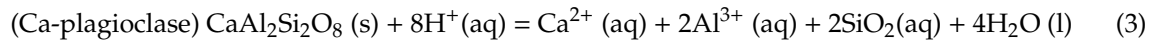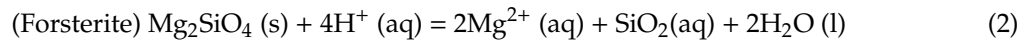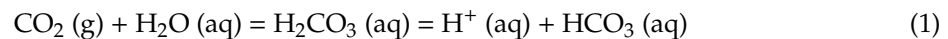
Numerous laboratory experiments have been performed to study the reactivity of olivine, serpentine, pyroxene, amphibole and plagioclase mineral groups, and glass basalt lavas with CO_2-enriched solutions [17–20]. Most of these experiments were conducted in batch conditions at controlled pressure, temperature and P_{CO_2}, using crushed rock. Sodium hydrogen carbonate ($NaHCO_3$) is often added in the reactor to increase the hydrogen carbonate concentration in solution and buffer the pH up to 7.7 and 8.0 [21]. This pH range, temperatures from 155 °C to 185 °C and total pressures from 11.5 MPa to 19 MPa [21–23] provide the optimal conditions for carbonation enhancement.

In general, the parameters that affect the rate of carbonate minerals' precipitation are brine composition, temperature, pressure and, principally, pH [24]. Mineral carbonation is favored over a higher pH—for instance, above 6.5 pH for Ca-Mg carbonates [25] or above 9.0 pH for $CaCO_3$ [9].

In the CarbFix project, the water in the Hellisheidi carbon injection site has a temperature ranging from 15 to 35 °C and the in situ pH ranges from 8.4 to 9.8 [26]. The injected water (with dissolved CO_2) has a temperature of 25 °C and a pH of 3.7 to 4.0 [27]. According to. [28], during the injection phase, the water with CO_2 will create porosity in the near vicinity of the injection by dissolving primary and secondary minerals. Furthermore, away from the injection well, secondary minerals will precipitate due to the reaction with the Ca-Mg-Fe-rich reservoir rocks.

Other authors [14,29,30] observed a decrease in the permeability of the carbonated rock. Inter- and intragranular pores (10 μm pore throats) were filled with magnesite and characterized using μRaman and SEM-TEM images. SEM-TEM observations [14] showed a magnesite layer separated from the olivine by submicron siderite grains, and poorly crystallized phyllosilicates. Iron oxide and amorphous silica are also observed as secondary phases in batch and flow-through experiments [14,22,29]. Phyllosilicates and chalcedony affect both the porosity and permeability, causing a decrease in the carbonation rate due to the creation of an exfoliated passivation layer rich in silica.

Carbonation experiments have been performed by [31] on continental flood basalt (CFB) samples (10.3 MPa and 90 °C) from eastern Washington, and by Schaef and McGrail [32] in basalt samples representing formations from North America, India and Africa.

Both studies noted that calcite was the first mineral to precipitate. For instance, Schaef and McGrail [32] observed small calcite nodules precipitating after 86 days. Post-reacted samples from Deccan basalts [32] displayed larger and opaque precipitates (after 280 days) and more reddish-brown grains containing a large calcite component (66.0–82.0 wt. %) and minor magnesite (9.1–22.0 wt. %) or siderite (3.1–15.0 wt. %) components. The basalt grains representing Southern Africa (Karoo) were insignificantly reactive, displaying very few carbonate nodules with high Mg (31.0 wt. %) and Fe (29.0 wt. %) contents. More recent basalt carbonation experiments have been performed by [33] on recent Auckland basalt (0.3 Ma). After 140-day experiments (100 °C and 5.5 MPa), they observed ankerite and aluminosilicates as secondary precipitation and an increase in both porosity and permeability. This observation contrasts with the major reported carbonation studies [29,30], where the permeability was observed to decrease due to carbonate growth. Theoretical and experimental studies of rock-CO_2 interactions in wet conditions and low temperature (25–90 °C) and first phases (0.5–100 days)

indicate the presence of chemical reactions and, consequently, textural-mineralogical-chemical changes [25]. However, according to [25], in order to optimize low-temperature mineral carbonations, an "equilibrium" between initial CO_2 (acid supply), rock to water ratio and temperature needs to be adjusted in order to effectively mineralize CO_2 within a reasonable time scale.

3. Methodology

To evaluate the potential for mineral carbonation in plutonic mafic rocks, a six-step methodology was followed (Figure 1):

1. Selection of representative samples for study and definition of conceptual conditions (rock-brine-CO_2) to be studied (Figures 1 and 2a).
2. Mineralogical, textural and chemical characterization of the specimens before exposure to brine and supercritical CO_2 (SC CO_2) (Figures 1 and 2b).
3. Exposure of the specimens to CO_2 supersaturated brine at selected conditions (supercritical CO_2: 8 MPa and 40 °C) in the autoclave (Figures 1 and 2c): (a) Stage 1—CO_2 pressurized injection (3 h); (b) Stage 2—CO_2 pressurized stabilization (1, 4, 16 and 64 days) and (c) Stage 3 CO_2—pressure release (3 h).
4. Upon conclusion of the laboratory experiments in Step 3, mineralogical, textural and chemical characterization of specimens and brine chemical analysis were conducted.
5. Geochemical modelling of the mineral carbonation experiments using CrunchFlow.
6. Interpretation of results and correlation of experimental and modelling data.
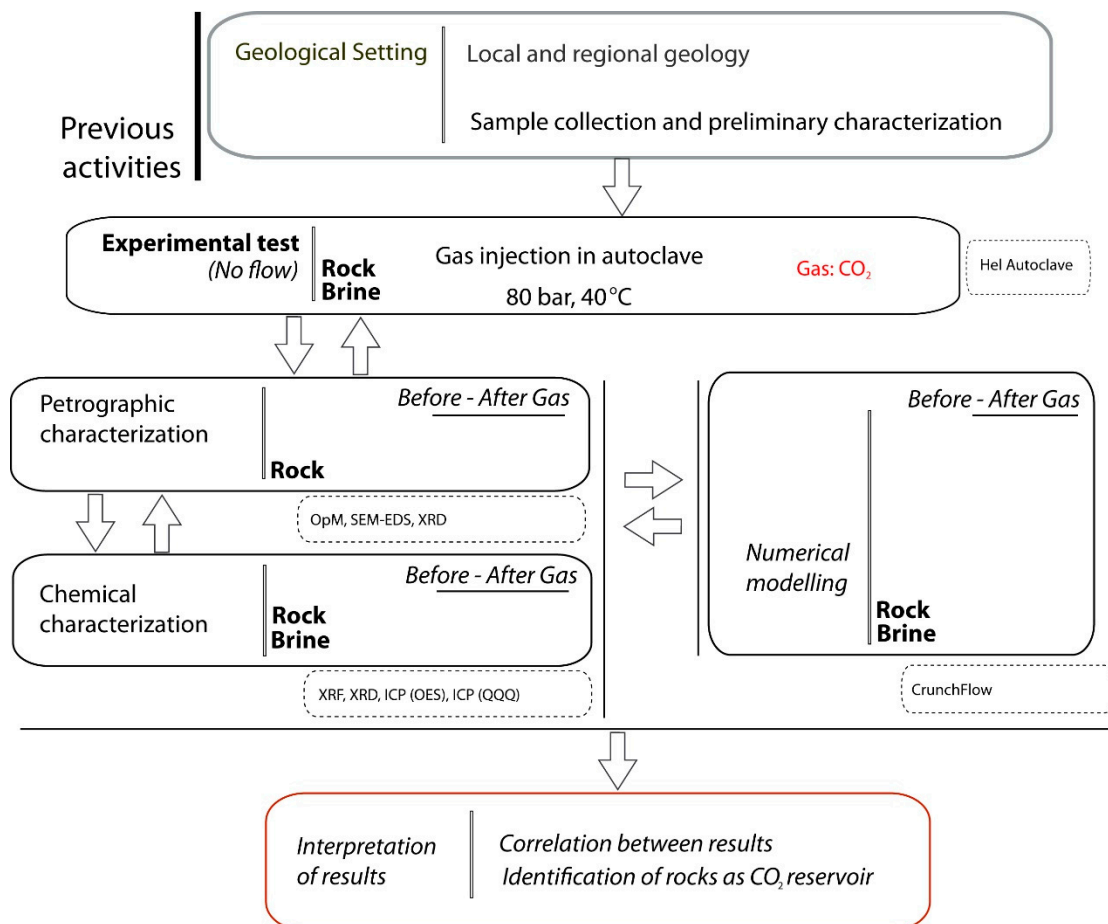
Figure 1. Schematic representation of the work sequence followed in this study.
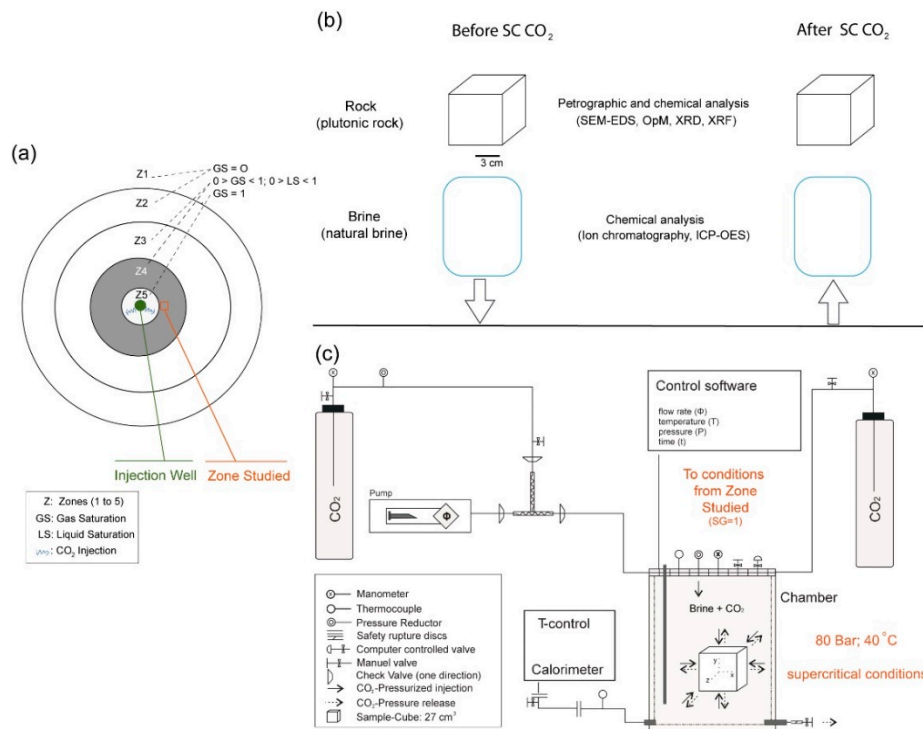
Figure 2. (**a**) Conceptual diagram of the reactive zones (Z1, Z2, Z3, Z4 and Z5) around the injection well according to [34] and [35]. (**b**) Sample preparation for mineralogical and geochemical analyses before and after SC CO_2 exposition. (**c**) Layout of the experimental setup. Reactor system used for the pressurized CO_2 injection (modified from. [36]).

3.1. Materials

Two different lithologies of igneous rock from the Sines Massif, Portugal were sampled and used in the experiments: (i) Experiment 1 with a cumulate gabbro (CG) from a cliff near Praia do Norte and (ii) Experiment 2 with a gabbro-diorite (GD) sampled at quarry Monte Chãos [11].

The CG displays a medium to coarse cumulate texture and is formed of clinopyroxene (45–55%), olivine (15–20%), brown amphibole (10–15%), plagioclase (5–10%) and primary ilmenite (5%); it occasionally shows accessory alteration products (e.g., chlorite, actinolite, serpentine). The GD exhibits a layered medium to coarse texture and is composed of plagioclase (50–60%), clinopyroxene (20–25%), subordinate olivine (5–10%), biotite (10–15%) and ilmenite (5–10%). Despite some fractures with chlorite and incipient sericitization, the sample has no significant alteration.

The coarse-grained CG sample was cut into 40 subsample cubes of 27 cm^3 each and four of 1 cm^3. They were divided in four run sets and one reference set (0-day set). For Experiment 1, each set of specimens had seven cubes of 27 cm^3, two parallelepipeds of 27/2 cm^3 and one of 1 cm^3 (Table 1). The coarse-grained gabbro-diorite sample was cut into 80 subsamples cubes of 27 cm^3 each and four of 1 cm^3. For Experiment 2, each set of specimens had 15 cubes of 27 cm^3, two parallelepipeds of 27/2 cm^3 and one of 1 cm^3 (Table 1).

Table 1. Experimental conditions of rock-brine-CO_2 exposure in autoclave.

Experiment	Sample	Samples of 27 cm^3	Samples of 27/2 cm^3	Samples of 1 cm^3	Brine (cm^3)	CO_2 (cm^3)	Run (Days)
1	Cumulate gabbro (CG)	7	2	1	600	1184	1, 4, 16, 64
2	Gabbro-diorite (GD)	15	2	1	1350	218	1, 4, 16, 64

The brine used in the experiments is a natural brine sampled from an old borehole in a saline aquifer (see Section 4.2).

3.2. Experimental Procedure (Autoclave)

The experimental setup of the autoclave employed in this experiment (Figure 2c) is based on similar systems described by [37] and [38]. Specific initial conditions in the autoclave were considered due to the planned target: sample material (rock-type and representative sample size), geological environment (pressure, temperature and salinity) and technical equipment (materials for chamber, software, pumps, etc.) for the final arrangement of the experimental device and run conditions. The autoclave (Figure 2c) [36,39] has two CO_2 cylinders (standard industrial CO_2 at 4.5 MPa) that are linked to the other elements of the system by steel connectors (diameter: 5 mm). The first CO_2 cylinder is directly connected with the chamber. The second CO_2 cylinder is connected to a piston pump that operates with a flow of 0.01 g/s. In case of gas leakage in the chamber during the experiment, this pump maintains the experimental pressure defined for the test. The inside of the chamber has a capacity of 2 dm^3. This is coated with polytetrafluoroethylene (PTFE) to protect the material against corrosion. At the bottom of the chamber, a thermostat controls the internal temperature. The calorimeter and pump are linked to the chamber with pressure and temperature sensors and are connected to a computer.

In detail, the experiment consisted of exposure of mafic rocks to CO_2-supersaturated brine (i.e., SC CO_2-rich brine) in the autoclave to a pressure (P) of 8 MPa and to a temperature (T) of 40 °C without flow. The P and T conditions were selected to exceed the CO_2 supercritical (SC CO_2) point [40,41] and to simulate the conditions of injection and storage of CO_2 [2,42]. These conditions are representative to a depth of approx. 800 m. The selected exposure time (1, 4, 16 and 64 days) was chosen to identify possible changes in the rock (dissolutions and/or precipitation) during the first injection phases.

The experiments began with the immersion of specimen rocks within natural brine in the chamber. Once the rock is introduced and fully immersed in the brine, CO_2 is injected (Table 1).

The experimental runs comprised: (a) a pressurized CO_2 injection (3 h, from 4.5 MPa and 20 °C conditions to the SC condition); (b) a pressurized stabilization (period of test, no CO_2 flow inside the chamber) and (c) CO_2 pressure release (3 h, from supercritical conditions to ambient conditions). The final volume of CO_2 in chamber to 80 bar and 40 °C was (i) 1184 cm^3 in experiment with CG and (ii) 218 cm^3 in experiment with gabbro-diorite. The times of filling and emptying the chamber with SC CO_2 were the same (3 h, from ambient conditions to supercritical conditions and supercritical conditions to ambient conditions, respectively), following the chamber manufacturer's recommendations. This is the time required to reach the target pressure and temperature values from the initial ambient conditions.

3.3. Material Characterization

To obtain a precise characterization of the rock specimens and to evaluate the changes after SC CO_2 exposure, in mineralogy, texture and chemistry, a set of complementary analytical techniques was repeatedly applied.

Petrography on thin-sections, by optical microscopy (OM), was performed by a Leica bright-field microscope (LEICA DM 2500P, Wetzlar, Germany).

The X-ray powder and in situ diffractograms were produced using a Bruker AXS-D8 Advance (Bruker Corp., Billerica, MA, USA), with Cu-Kα radiation (λ = 0.1540598 nm), under the following conditions: scanning between 3° and 75° (2θ), scanning velocity of 0.05° 2θ/s, accelerating voltage of 40 kV, and current of 40 mA. In order to evaluate the mineralogical composition of the specimen surface, in situ grazing incidence geometry experiments were conducted, with incidence of 1.5° and 2θ scanning from 8 to 60°.

A Hitachi S-3700N SEM (Hitachi High Technologies, Berlin, Germany), coupled with a Bruker XFlash 5010 SDD detector (Bruker Corp, Billerica, MA, USA), was used for the surface sample chemical analysis. The analysis was performed under a low vacuum at 40 Pa, with a current of 20 kV. An infrared spectrometer Bruker Hyperion 3000 equipped with a single-point MCT detector cooled with liquid nitrogen and a 20 × ATR objective with a Ge crystal of 80 μm diameter was used.

An infrared spectrometer Brüker Hyperion 3000 equipped with a single-point MCT detector cooled with liquid nitrogen and a 20 × an attenuated total reflectance (ATR) objective with a Ge crystal

of 100 μm diameter was used. The infrared spectra were acquired with a spectral resolution of 4 cm^{-1}, 32 scans, in the 4000-650 cm^{-1} region. In order to ensure the representativeness of the data, each cube was analysed in nine different spots, screening the most exposed surface, and each spot was analysed three times.

The whole-rock geochemistry analysis was provided by XRF, which allows for the quantification of major oxides (SiO_2, TiO_2, Al_2O_3, Na_2O, K_2O, CaO, MgO, MnO, FeO, P_2O_5), sulfur and some minor elements (Rb, Sr, Y, Zr, Nb, Th, Cr, Co, Ni, Cu, Zn, Ga, As, Pb, Sn, V, U, Cl). Analyses were performed with an S2 Puma energy-dispersive X-ray spectrometer (Bruker), using a methodology similar to that adopted by [43]. A description of the standard reference materials (SRM) utilized in the calibration method can be found elsewhere [44]. After the determination of loss on ignition (LOI), samples were fused on a Claisse LeNeo heating chamber, using a flux (Li-tetraborate) to prepare fused beads (ratio sample/flux = 1/10). The software utilized for acquisition and data processing was Spectra Elements 2.0, which reported the final oxide/element concentrations and the instrumental statistical error (Stat. error) associated to the measurement.

OM, XRD, XRF, FTIR and SEM-EDS analyses were performed at HERCULES Laboratory (University of Évora, Portugal).

Linear roughness was measured by a homemade microprofilometer consisting of 55 parallel needles put in contact. The spacing between the needles' center-line is 500 μm for a total measurable length of 3.5 mm. After the profile measure, a photo of the needles' position was taken. Profiles of the samples were detected by drawing a line joining all the extremities of the needles, with the help of Adobe Photoshop CC 2018. The profile line in JPG format was uploaded on online software (WebPlotDigitizer, https://apps.automeris.io/wpd/) that allowed us to identify the X and Y values of the line according to the pixels composing the JPG photo. Pixel values were later converted to microns according to a scale.

The brine analyses were performed at IGME (Madrid, Spain) by ion chromatography (Dionex 600 de Vertex) and ICP-OES (Varian Vista MPX) before and after the experiment on each run. Iron and magnesium brine content determination, from Experiment 1, was performed at HERCULES Laboratory (Évora, Portugal) with an Agilent 8800 ICP Triple Quad (ICP-QQQ), operating with an RF power of 1550 W, RF matching of 1.7 V, a sample depth of 10 mm, carrier gas (Ar) of 1.1 L/min and plasma gas (Ar) of 15 L/min. Prior to the analysis, the equipment was calibrated with a tuning solution from Agilent, and the sensitivity and resolution were optimized and the doubly charged ions (< 1.84%) and oxides (< 1.10%) were minimized.

3.4. Geochemical Modelling

3.4.1. Code Descriptions and Capabilities

The simulations were performed using CrunchFlow [45,46], a multicomponent reactive flow and transport code for studying fluid rock interactions in porous media. The reactive transport code has many advantages such as a complete equilibrium thermodynamic treatment, flexible kinetic rate law formulations for each mineral depending on the reaction mechanism, and a range of 3D flow capabilities. The reactive transport code [47] numerically solves the mass balance of solutes, as shown in Equation (7):

$$\frac{\partial(\phi C_j)}{\partial t} = \nabla \cdot (D \nabla C_j) - \nabla(q C_j) + R_j \ (j = 1, 2, 3 \ldots n) \tag{7}$$

where ϕ is the updated porosity, C_j is the concentration of component j (mol m^{-3}), q is the Darcy velocity (m s^{-1}), R_j is the total reaction rate affecting component j (mol m^{-3} s^{-1}) and D is the combined

dispersion-diffusion coefficient ($m^2 s^{-1}$). The carbonation experiments were conducted in closed batch conditions, that is, without flow, so that Equation (7) can be simplified as Equation (8):

$$\frac{\partial(\phi C_j)}{\partial t} = R_j \ (j = 1, \ 2, \ 3 \ldots n) \tag{8}$$

The reaction rate is only described as function of time. The mineral dissolution to aqueous phases and precipitation of secondary phases are kinetically controlled, thus a reaction rate is given in term of primary species. The reaction kinetic is treated based on the rate law types including the transition state theory (TST), irreversible, monod, dissolution only and precipitation only [46]. In this work, a common theoretical framework provided by the TST rate law [48–50] is adopted. The dissolution and precipitation are treated as reversible at equilibrium, by explicitly including a dependence on Gibbs energy or saturation state (Equation (9)):

$$R_m = \mp A_m k_m \left(\prod a_n\right) \left|\left(\frac{Q_m}{K_{eq}}\right)^n - 1\right|^m \tag{9}$$

where R_m is the rate of precipitation (rate > 0) or dissolution (rate < 0) of mineral m in mol $L^{-1} s^{-1}$, A_m is the reactive surface area and k_m the kinetic constant of mineral m (in $mol.m^{-2}.s^{-1}$). The sign of the saturation index $\Omega = \log\left(\frac{Q_m}{K_{eq}}\right)$ determines the sign of the reaction rate. Negative means dissolution and positive means precipitation. The kinetic constant at given temperature *T (K)* is calculated from Equation (10):

$$k = k_{25} \mathrm{Exp}\left[\frac{E_a}{R}\left(\frac{1}{T} + \frac{1}{298.15}\right)\right] \tag{10}$$

where k_{25} is the kinetic constant at 25 °C, E_a is the apparent activation energy (KJ mol^{-1}) and R is the gas constant (J $mol^{-1}K^{-1}$). The change in initial porosity (ϕ_i) and mineral bulk surface area (A_m) owing to dissolution is computed from Equation (11):

$$A_m = A^{\mathrm{initial}} \left(\frac{\phi_m}{\phi_{(i)m}}\right)^{\frac{2}{3}} \left(\frac{\phi}{\phi_i}\right) \tag{11}$$

and the change due to precipitation is computed from Equation (12):

$$A_m = A^{\mathrm{initial}} \left(\frac{\phi}{\phi_i}\right). \tag{12}$$

3.4.2. Input Conditions for Rock and Fluid Composition

The numerical simulations presented in this article only describe the CG experiments; modelling of the gabbro-diorite experiments is ongoing and will be described elsewhere. The initial mineral composition of the rock was derived from Canilho [51] and adjusted with petrography and mineral chemistry, obtained through SEM-EDS [11]. For the numerical simulations, it was assumed that CG is mainly composed of clinopyroxene and olivine, associated with minor amounts of amphibole and calcic plagioclase. Iron oxides and small retrogradation mineral phases were not considered. As in the autoclave experiments, the modelling considered a closed system in which the solid rock takes 20% of the volume and the remaining space is taken up by the brine. As a requirement of the code database, the CG mineral phases are described with the endmembers of the solid solutions, as represented in Table 2. The reactive surface area for each mineral was calculated based on a random variable of the specific surface areas (SSA), defined in the literature as ranging from 10 to 250 cm^2/g (e.g.,

applying Brunauer-Emmett-Teller (BET) measurements) for mafic and ultramafic rock [25,52–56] from Equation (13):

$$A_{bulk} = \frac{\varphi_m SSAM_w}{V_m} + SA. \tag{13}$$

Table 2. Considered modal composition assumed for cumulate gabbro modelling and reactive surface area considered for the calculations.

Rock Composition	Vol. Fraction (%)	10 cm²/g	75 cm²/g	120 cm²/g	170 cm²/g	220 cm²/g
		Reactive Surface Area (m²/m³) (or $A_{initial}$)				
Albite, $NaAlSi_3O_{8)}$	0.35	9.15	68.65	1.09×10^2	1.55×10^2	2.01×10^2
Anorthite, $CaAl_2Si_2O_8$	3.25	88.32	6.62×10^2	1.06×10^3	1.5×10^3	1.94×10^3
Diopside, $CaMgSi_2O_6$	10.8	3.53×10^2	2.64×10^3	4.23×10^3	5.9×10^3	7.76×10^3
Forsterite, Mg_2SiO_4	2.42	77.1	5.78×10^2	9.25×10^2	1.31×10^3	1.69×10^3
Fayalite, Fe_2SiO_4	2.21	96.63	7.24×10^2	1.16×10^2	1.64×10^3	2.12×10^3
Enstatite, $MgSiO_3$	0.56	19.97	1.34×10^2	2.15×10^2	3.05×10^2	3.95×10^2
Ferrosilite, $FeSiO_3$	0.41	16.0	1.2×10^2	1.92×10^2	2.72×10^2	3.52×10^2
Φ (brine fraction)	80					
Total	100					

The term SA (geometric surface area = 0.67 cm²/g) is the ratio between the rock area and the rock volume = 1.68 cm²/cm³. Because the dissolution reactions depend on the minerals' surface areas, we adjusted the SA with the first term in Equation (13), in order to reproduce the ideal conditions for CO_2 mineralization. In fact, mineral surface area is the most uncertain and complex kinetic parameter and the evolution (especially for multimineral systems) is not quantitatively understood at present [53]. The definition of this parameter requires random values as the measured values using BET overestimates the reaction rates [53,55,57].

The kinetic constants for the reacting minerals were taken from the literature [52,53]. The fit of the model to the experimental data (aqueous calcium, silica, magnesium and iron) concentrations and pH) was performed based on Table 2. The initial concentration of dissolved CO_2 was calculated to be 5.5×10^{-1} mol kgw^{-1} according to the Duan and Sun [16] model, with an imposed total pressure of 80 bars. From the thermodynamic and kinetic point of view, 73 aqueous species were considered in the simulations. The equilibrium constants were taken from the EQ3/6 thermodynamic database [58] included in CrunchFlow. The activity coefficients were calculated using the extended Debye-Hückel formulation (b-dot model) [59], with parameters from the same database. The brine composition in the simulations is similar to that of the brine used in the experiments, with pH = 6.85 (before CO_2 addition). The brine is enriched in Ca and Mg (5.12×10^{-2} and 2.62×10^{-2} mol.kgw^{-1}) and contains important amounts of sulfur and sodium chloride (Table 3).

Table 3. Chemical composition of solution used as input in the simulation.

Components	(mg kgw^{-1})	(mol kgw^{-1})
Ca^{2+}	2050	5.12×10^{-2}
Mg^{2+}	560	2.33×10^{-2}
Fe^{2+}	5.16	1.01×10^{-4}
SiO_2(aq)	11.5	1.55×10^{-4}
K^+	260	6.64×10^{-3}
Na^+	85,450	3.7
SO_4^{2-}	5400	5.62×10^{-2}
Cl^{-1}	133,500	3.56

4. Results

4.1. Petrographic and Chemical Characterisation of Rocks before and after SC CO_2 Exposure

The two lithologies (CG and GD) used in experiments and tested as described above show similar textural and mineralogical results. After interaction of the rock specimens with the SC CO_2

supersaturated brine in the autoclave chamber, an increase in the dissolution of specimens can be perceived; after the one-day run there is a noticeable surface roughness, which increases for the longer runtimes and eventually leads to material fragmentation for 16-day and 64-day runs (Figure 3). The mean linear roughness (Ra) is higher on CG from 14.80 μm to 21.89 μm for 16 and 64 days, respectively, whereas for GD the Ra increases from 1.01 μm to 1.85 μm for 16 and 64 days, respectively.

Figure 3. Stereo-zoom image that displays the effect of minerals dissolution (arrow) on the surface of a gabbro-diorite specimen after 64 days within brine.

The petrographic analyses, through transmitted light microscopy, did not show significant mineralogical or textural differences after the experiments. It is important to note that even if there were any changes, they should be located on the surface and the thin section production process could have eliminated them. The powder-XRD performed on global fraction before immersion [11] reflects the modal igneous composition given by clinopyroxene, olivine, amphibole, plagioclase and magnetite for CG and plagioclase, clinopyroxene, olivine and mica for the GD (Table 4). Clinochlore has been identified on both rock samples and probably derived from the alteration of the mafic mineralogical phases. After the 1-, 4-, 16- and 64-day runs, the obtained powder diffractograms (Table 4) shows besides the igneous mineralogy the new presence of talc, vermiculite, and halite on both CG and GD in most specimens. Moreover, XRD performed on the surface of CG and GD 64-days specimens, through grazing incidence (Figure 4), additionally reveals the presence of smectite and gypsum, which were not detected in 0-day specimens.
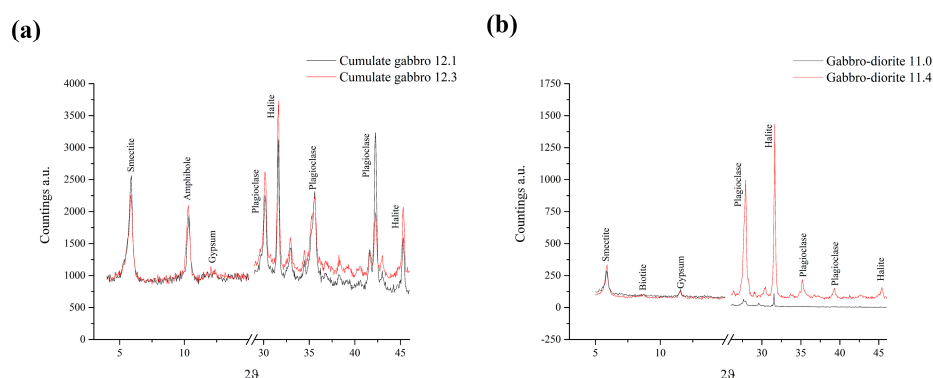
Figure 4. Diffractograms obtained through grazing apparatus on specimens after 64 days within brine: (**a**) cumulate gabbro; and (**b**) gabbro-diorite. For each we present diffractograms obtained at two distances, where the highest value is nearest the surface of the specimen.

Table 4. Mineralogical composition obtained through powder XRD. Tr: trace amount.

	Sample/Days	Clinopyroxene	Amphibole	Plagioclase	Clinochlore	Vermiculite	Talc	Mica	Olivine	Halite	Rutile	Ilmenite	Magnetite
Experiment 1	CG_0	32	24	13	4			2	5				2
	CG_1	38	28	17	4		Tr	3	8	1			2
	CG_4	26	29	24	4	Tr	Tr	3	10	1			2
	CG_16	37	21	21	3	Tr	Tr	2	12	1			2
	CG_64	34	24	26	3	Tr	Tr	2	8	1			2
Experiment 2	GD_0	16	4	69	Tr			6	3			3	
	GD_1	12	4	73	1		Tr	5	1	1		2	
	GD_4	12	4	73	1	Tr	Tr	5	1	1		2	
	GD_16	10	5	73	1	Tr	Tr	5	1	1	1	1	
	GD_64	16	4	69	2		Tr	4	2	1		1	

As described for the CG [60], the SEM images obtained before and after each experiment on GD (Figure 5a,b) essentially show an increase in ferromagnesian minerals' dissolution, reflected in the higher surface roughness, as reported by other authors [61]. The added phases show different reflectance on backscattered electron (BSE) images and, according to EDS elemental map distribution (Figure 5c,d), correspond to significant enrichment in chlorine (Cl), sodium (Na), sulfur (S) and carbon (C). The precipitation of salts in the form of efflorescence covers a large part of the surface of the specimens and the cavities generated by the dissolution.
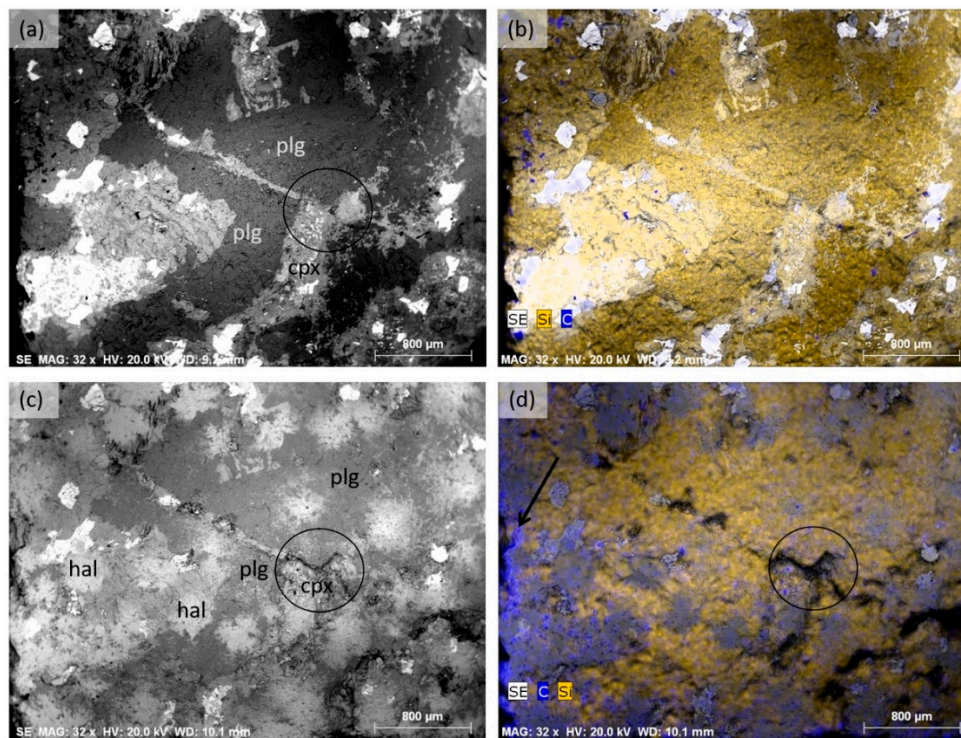
Figure 5. SEM images of a gabbro-diorite specimen before (upper) and after (lower) SC CO_2 brine: (**a**) backscattered electron (BSE) images at 0 days; (**b**) BSE and EDS elemental maps distribution for silicon and carbon at 0 days; (**c**) BSE images after 64 days; and (**d**) BSE and EDS elemental maps distribution for silicon and carbon after 64 days, with preferential dissolution of clinopyroxene (circle) and carbon enrichment (organic accumulation) on the edge of specimen (arrow). plg—plagioclase, cpx—clinopyroxene, hal—halite.

The carbon enrichment observed on the edge of 64-day specimens (CG and GD) and associated with salts (Figures 5d and 6a) corresponds to organic material, which accumulates due to runoff during the drying process at 40 °C. The origin of this material remains to be identified, but is probably related to the presence of organic material (hydrocarbon) within the original brine.

In fact, the carbon particles observed at the surface (Figure 6a) are not related to the crystallization of carbonates or any other mineral phase [60]. The ATR-FTIR spectra of these carbon-enriched areas present infrared fingerprints pointing to the presence of triglyceride-enriched areas whose origin is still to be determined [58]. In addition, the analysis by ATR-FTIR of CG and GD after 16 days (Figure 6b) of interaction with CO_2 revealed a decrease in the intensity of the absorption band

Whole-rock geochemistry data for CG and GD before and after 64 days within a SC CO_2-brine solution are shown in Table 5. For CG the most significant variations after a six-day run were an increase in CaO (+0.4 wt. %) and a decrease in Fe_2O_3 (−0.4 wt. %), whereas in GD CaO and Fe_2O_3 decreased ((−0.42 wt. % and (−0.3 wt. %, respectively). The enrichment in sodium was more evident in GD specimens after 64 days within SC CO_2-brine (+0.13 wt. % vs. 0.04 wt. % for CG). Sulfur increased in both samples after 64 days (+0.05 wt. % and +0.08 wt. % for GB and GD, respectively).
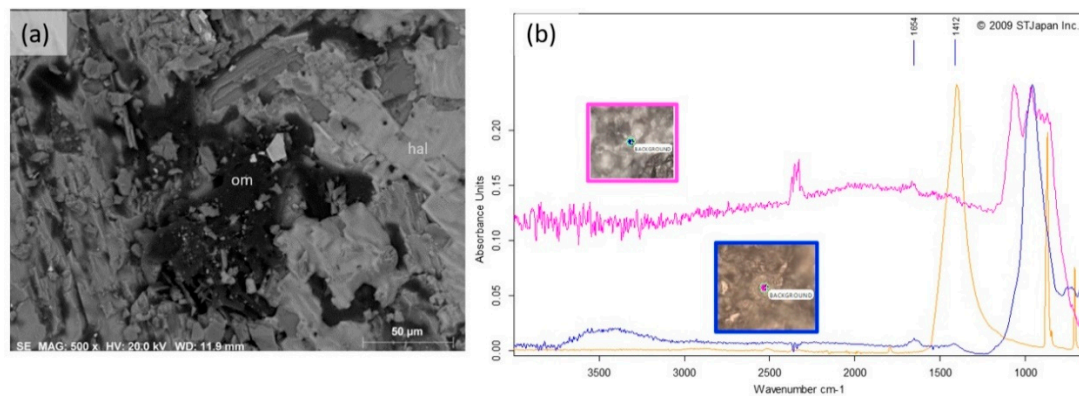
Figure 6. (**a**) Backscattered electron image of a detail of carbon-rich particles (om—organic matter) associated with halite (hal); (**b**) ATR-FTIR spectra of gabbro-diorite (GD) at 0 days (blue) and 16 days (pink). The calcite reference spectrum is also shown for comparison (yellow; STJapan Inc. database). The insets are the spots of analysis.

Table 5. Whole-rock geochemistry before and after runs of 64 days for cumulate gabbro (CG) and gabbro-diorite (GD).

	CG 0 (wt. %)	Stat. Error	CG 64 (wt. %)	Stat. Error	GD 0 (wt. %)	Stat. Error	GD 64 (wt. %)	Stat. Error
SiO_2	42.30	± 0.0344	42.20	± 0.0345	49.00	± 0.0356	49.50	± 0.0356
TiO_2	3.34	± 0.0175	3.20	± 0.0175	3.26	± 0.0176	3.16	± 0.0176
Al_2O_3	9.40	± 0.0295	9.50	± 0.0300	16.20	± 0.0368	16.40	± 0.0369
Fe_2O3	15.50	± 0.0133	15.10	± 0.0135	11.20	± 0.0115	10.90	± 0.0115
P_2O_5	0.28	± 0.00427	0.34	± 0.00439	0.85	± 0.00506	0.74	± 0.00494
MnO	0.40	± 0.005	0.40	± 0.005	0.32	± 0.005	0.31	± 0.005
MgO	12.90	± 0.0506	12.80	± 0.0503	4.48	± 0.0349	4.27	± 0.0344
CaO	12.70	± 0.0428	13.10	± 0.0444	8.33	± 0.0375	7.91	± 0.0371
BaO	0.23	± 0.013	0.20	± 0.013	0.28	± 0.013	0.27	± 0.013
Na_2O	0.84	± 0.0519	0.88	± 0.0512	3.46	± 0.0607	3.59	± 0.0612
K_2O	0.19	± 0.0345	0.23	± 0.0356	1.42	± 0.0395	1.42	± 0.0396
S	0.19%	± 0.00172	0.24%	± 0.00178	0.15%	± 0.00162	0.23%	± 0.00174
LOI	0.89		0.95%		0.03%		0.25%	
total	99.17		99.14%		98.98%		98.95%	
	(ppm)		(ppm)		(ppm)		(ppm)	
Rb	9	± 2.08	10	± 2.14	40	± 2.24	39	± 2.27
Sr	286	± 2.57	313	± 2.67	748	± 3.09	763	± 3.13
Y	15	± 2.30	15	± 2.37	34	± 2.46	35	± 2.49
Zr	80	± 2.82	74	± 2.90	199	± 3.14	208	± 3.19
Nb	20	± 2.52	14	± 2.60	62	± 2.65	65	± 2.68
Th	9	± 2.94	13	± 3.02	10	± 3.10	10	± 3.15
Cr	478	± 29.0	526	± 30.5	20	± 25.4	65	± 25.9
Co	198	± 5.65	198	± 5.76	139	± 5.02	134	± 5.00
Ni	117	± 4.12	135	± 4.29	7	± 3.42	14	± 3.54
Cu	62	± 4.82	64	± 4.91	42	± 4.88	49	± 5.01
Zn	103	± 6.07	100	± 6.19	108	± 6.37	101	± 6.26
Ga	14	± 4.30	15	± 4.41	25	± 4.67	19	± 4.70
As	7	± 4.29	2	± 4.39	8	± 4.53	10	± 4.61
Pb	0	± 0	2	± 16.7	12	± 17.2	0	± 0
Sn	7	± 27.3	0	± 0	0	± 0	13	± 28.0
V	479	± 68.0	505	± 68.9	323	± 68.0	249	± 67.8
U	0	± 0.209	1	± 0.215	2	± 0.221	2	± 0.225
Cl	43	± 0.364	54	± 0.371	53	± 0.359	70	± 0.383

4.2. Brine Evolution

Before starting the carbonation experiments, the composition of the brine was analysed using a combination of techniques (see Tables 6 and 7, "Pure Brine" column). The brine used in each run of experiments was recovered immediately after the end of the run for a comparative chemical analysis.

Table 6. Chemical analysis of pure brine and brine taken from the reaction chambers (one, four, 16 and 64 days) for Experiment 1 with CG (Figure S1 as supplementary material).

	Pure Brine (mg/L)	Brine Post Test (mg/L)	Brine Post Test (mg/L)	Brine Post Test (mg/L)	Brine Post Test (mg/L)
	0 Days	1 Day	4 Days	16 Days	64 Days
Na^+	85.45×10^3 $\pm 11.96 \times 10^3$	67.11×10^3 $\pm 93.96 \times 10^3$	86.02×10^3 $\pm 12.04 \times 10^3$	84.05×10^3 $\pm 11.77 \times 10^3$	79.68×10^3 $\pm 11.16 \times 10^3$
K^+	260 ± 31	260 ± 31	305 ± 37	310 ± 37	415 ± 50
Mg^{2+}	560 ± 100	590 ± 106	590 ± 106	610 ± 109	680 ± 122
Ca^{2+}	2050 ± 205	1900 ± 190	1890 ± 189	1860 ± 186	1650 ± 165
SO_4^{2-}	5400 ± 756	5400 ± 756	5600 ± 784	5700 ± 798	5300 ± 742
Cl^-	13.35×10^4 $\pm 1.6 \times 10^4$	10.40×10^4 $\pm 1.3 \times 10^4$	13.3010^4 $\pm 1.6 \times 10^4$	12.40×10^4 $\pm 1.5 \times 10^4$	11.90×10^4 $\pm 1.4 \times 10^4$
HCO^-_3	40 ± 4.0	35 ± 3.5	38 ± 3.8	35 ± 3.5	33 ± 3.3
Fe (total)	5.2 ± 0.3	6 ± 0.3	11.3 ± 0.6	18.9 ± 0.9	26.4 ± 1.3
NO^-_3	0	0	0	0	0
SiO_2	11.5 ± 1.2	20 ± 2.8	24.9 ± 3.5	39 ± 5.5	37 ± 5.2
pH (pH Unit.)	6.9 ± 0.2	4.5 ± 0.1	4.9 ± 0.1	5.1 ± 0.2	5.5 ± 0.2
Cond (mS/cm)	80,000	85,000	80,000	75,000	75,000

Table 7. Chemical analysis of pure brine and brine taken from the reaction chambers (1, 4, 16 and 64 days) with GD (Figure S2 as supplementary material).

	Pure Brine (mg/L)	Brine Post Test (mg/L)	Brine Post Test (mg/L)	Brine Post Test (mg/L)	Brine Post Test (mg/L)
	0 Days	1 Day	4 Days	16 Days	64 Days
Na^+	87.61×10^3 $\pm 12.26 \times 10^3$	10.25×10^3 $\pm 14.35 \times 10^3$	99.72×10^3 $\pm 13.96 \times 10^3$	$10.70 \times 10^3 \pm$ 14.98×10^3	$78.54 \times 10^3 \pm$ 11.00×10^3
K^+	235 ± 28.2	250 ± 30	240 ± 28.8	270 ± 32.4	275 ± 33
Mg^{2+}	580 ± 116	560 ± 112	560 ± 112	580 ± 116	600 ± 120
Ca^{2+}	1520 ± 152	1640 ± 164	1680 ± 168	1660 ± 166	1650 ± 165
SO_4^{2-}	6900 ± 966	7200 ± 1008	7300 ± 1022	7600 ± 1064	6400 ± 896
Cl^-	9.70×10^4 $\pm 1.2 \times 10^4$	11.70×10^4 $\pm 1.4 \times 10^4$	12.70×10^4 $\pm 1.5 \times 10^4$	11.20×10^4 $\pm 1.3 \times 10^4$	11.10×10^4 $\pm 1.3 \times 10^4$
HCO^-_3	40 ± 4	40 ± 4	50 ± 5	110 ± 11	100 ± 10
NO^-_3	0	0	0	0	0
SiO_2	8 ± 0.8	10 ± 1	39 ± 3.9	59 ± 5.9	19 ± 1.9
pH (pH Unit.)	7 ± 0.2	5 ± 0.2	5.2 ± 0.2	5.4 ± 0.2	5.6 ± 0.2
Cond. (mS/cm)	80,000	77,500	77,000	77,000	80,000

The variation in the brine chemistry with time for both experiments—Experiment 1 with CG and Experiment 2 with GD—is shown in Tables 6 and 7. The pH, measured just after concluding each run, is more acidic for Experiment 1 (with CG). In fact, the initial pH of 6.85 dropped to 4.5, 4.87, 5.1 and 5.5, after one, four, 16 and 64 days, respectively, in the brine-rock-CO_2 system (Table 1) whereas for Experiment 2 (with GD) the pH decreased from 7 (brine without CO_2) to 5.81, 5.61, 6.38 and 6.61. In Experiment 2, the number of specimens was doubled (higher rock/brine ratio), but there was not a clear increase in the concentration of ions in solution, as suggested by similar values of conductivity for both experiments.

For Experiment 1 (CG), in general, the behavior of cations in solution was variable, despite the tendency of Ca^{2+} decreasing, whereas K^+, Mg^{2+}, SiO_2 and total Fe increased.

For Experiment 2 (GD), besides Na^+, all other analysed cations had lower concentrations in solution when compared to Experiment 1. Furthermore, the analysed elements did not always show the same behavior as described for Experiment 1. After an increase until the four-day run,

Ca^{2+} tended to stabilize. K^+ showed an increase, whereas Mg^{2+} concentrations tended to stay the same or increase slightly. SiO_2 clearly increased, but the 64-day run saw a decrease in silica.

In both experiments, SO_4^{2-} had similar behavior: a smooth enrichment, followed by a decrease for the 64-day run; Na^+ and Cl^- had more unpredictable behavior, displaying either enrichment or impoverishment trends along the four runs.

4.3. Geochemical Modelling of Experiments with Cumulate Gabbro

4.3.1. Outlet Solution Composition

The results of the experimental and simulated variations and tendencies in the output concentration over time are shown in Figure 7. The measured and simulated pH in brine supersaturated with CO_2 are presented as a function of the reactive surface area (Figure 7a) and compared to the variation of dissolved CO_2 (Figure 7b).
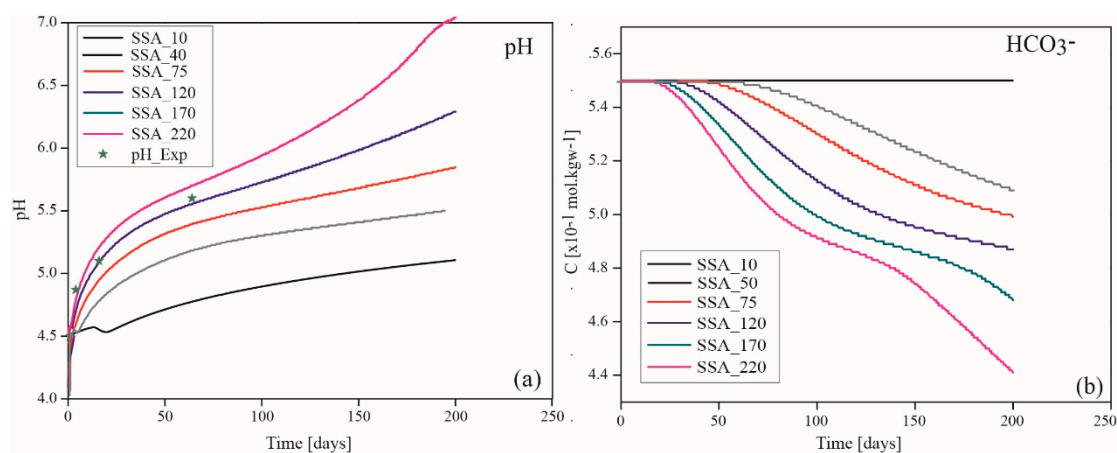
Figure 7. (**a**) Simulated pH variations of the outlet fluid compared with the measured pH; (**b**) simulated dissolved CO_2 (as HCO_3^-) variations as a function of time computed with different specific surfaces. The measured HCO_3^- values are obtained after opening the chamber and are not relevant for comparison.

Initially, the fluid pH at the onset of the modelling was 4.0 and increased rapidly to 4.5, and then gradually to 7.0, in the range of the measured values. Clearly, over the simulated time (0 to 200 days), pH ranged from 4.0 to 5.1 for the low SSA, increasing up to 7 for high SSA (170–220 $cm^2.g^{-1}$). The interaction between the rock and acidified fluid is a function of the dissolved CO_2 and the reactive surface area, since the decrease in HCO_3^- is inversely correlated to the increase in pH. Hence, the increase in pH above 5.5 was correlated to the consumption of the dissolved CO_2. As a result, at t < 50 days for SSA < 75 $cm^2.g^{-1}$, and t < 10 days, for SSA = 170–220 $cm^2.g^{-1}$, the pH remains lower than 5.0 and the dissolved CO_2 concentration remained constant. The constant concentration of HCO_3^- at a low pH denotes a dominant dissolution phase, where the concentration of the primary aqueous species (Ca, Mg, Fe, SiO_2) increases with time (Figure 8). However, at moderate and high pH values, CO_2 consumption is inferred from the decline in HCO_3^- concentration (below 0.48 $mol.kgw^{-1}$), triggering CO_2 mineralization into carbonates.

Simulated aqueous silica, Ca, Mg and Fe were observed to initially increase and then level off or decrease over increasing time. For instance, a minor increase in Ca concentration with respect to the initial concentration ($\Delta C_{Ca} = 0.14$ $mol \cdot kgw^{-1}$) was observed for t < 40 days before a continuous decrease began. The pattern of increase and decrease match perfectly with the evolution of dissolved CO_2, and are in agreement with the observations in previous studies [14,25,29,55].
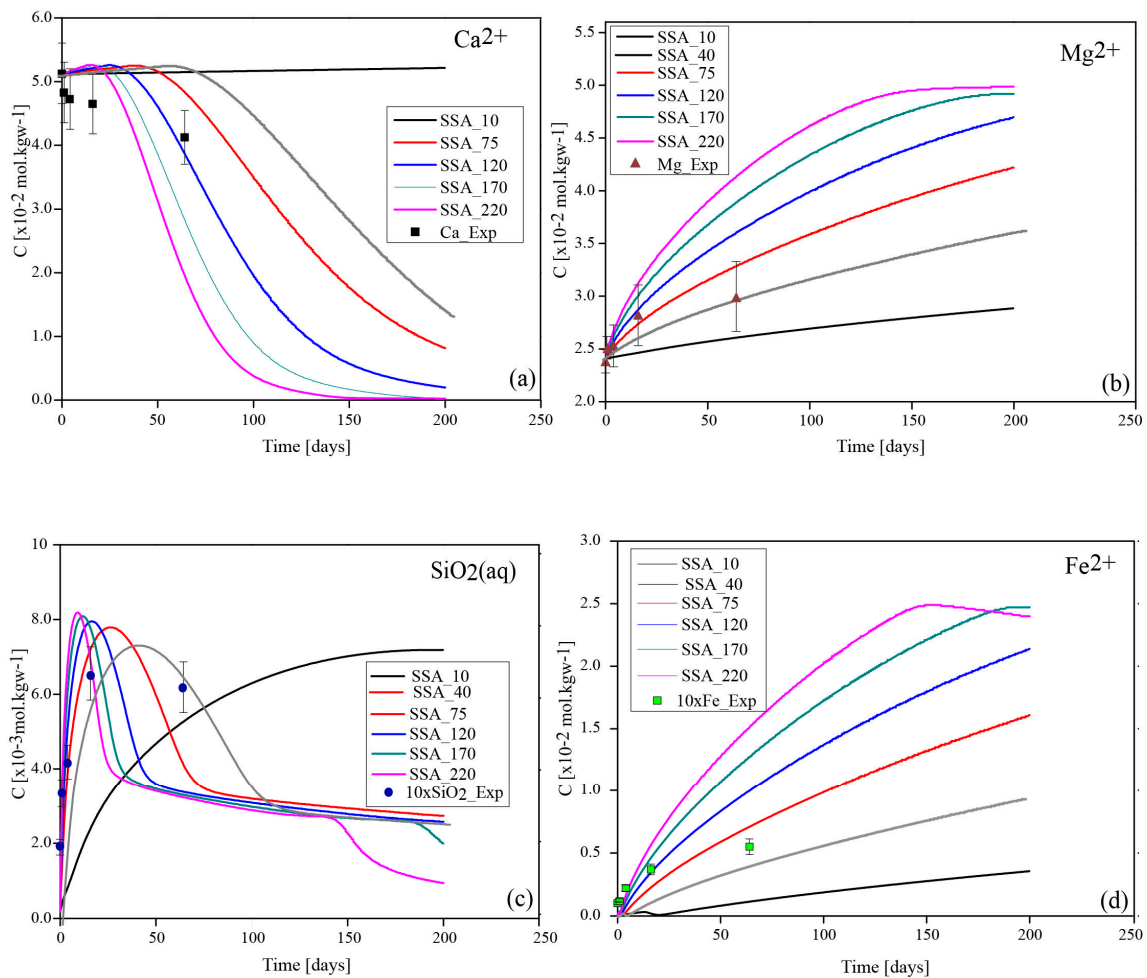
Figure 8. Variation in the solution composition with time compared to the experimental data. (**a**) Ca^{2+}; (**b**) Mg^{2+}; (**c**) $SiO_2(aq)$; (**d**) Fe^{2+}.

The simulated magnesium concentration doubled before levelling off (after 100 days). Moreover, the $SiO_2(aq)$ concentration stabilized shortly before a sharp and progressive decrease, indicating quantitatively important secondary silicate phases' precipitation. A steady increase in iron concentration was observed; the simulation indicates levelling off occurred later, after 150 days, and was attributed to fayalite dissolution. Aluminum values, initially 1.0×10^{-4} mol/kg, dropped sharply by five orders of magnitude, following the albite, Ca zeolite and kaolinite precipitation observed in the first simulation.

Because of the assumptions made in the initial mineralogy, the simulation could not reproduce the potassium and $SO4^-$ behaviors.

4.3.2. Minerals' Dissolution and Precipitation

Simulated primary and secondary minerals saturation indices (SI) are shown in Figure 9a,b. All primary minerals (except albite) are seen to dissolve (negative saturation index and rate, Table 3). SI of albite remains positive over time, implying that the modest decrease in Na^+ (from 0.371 to 3.69 mol.kgw^{-1}) is a consequence of albite volume increase. The dissolution rates (Table 8) indicate that olivine, plagioclase and diopsidic minerals are the most reactive phases.
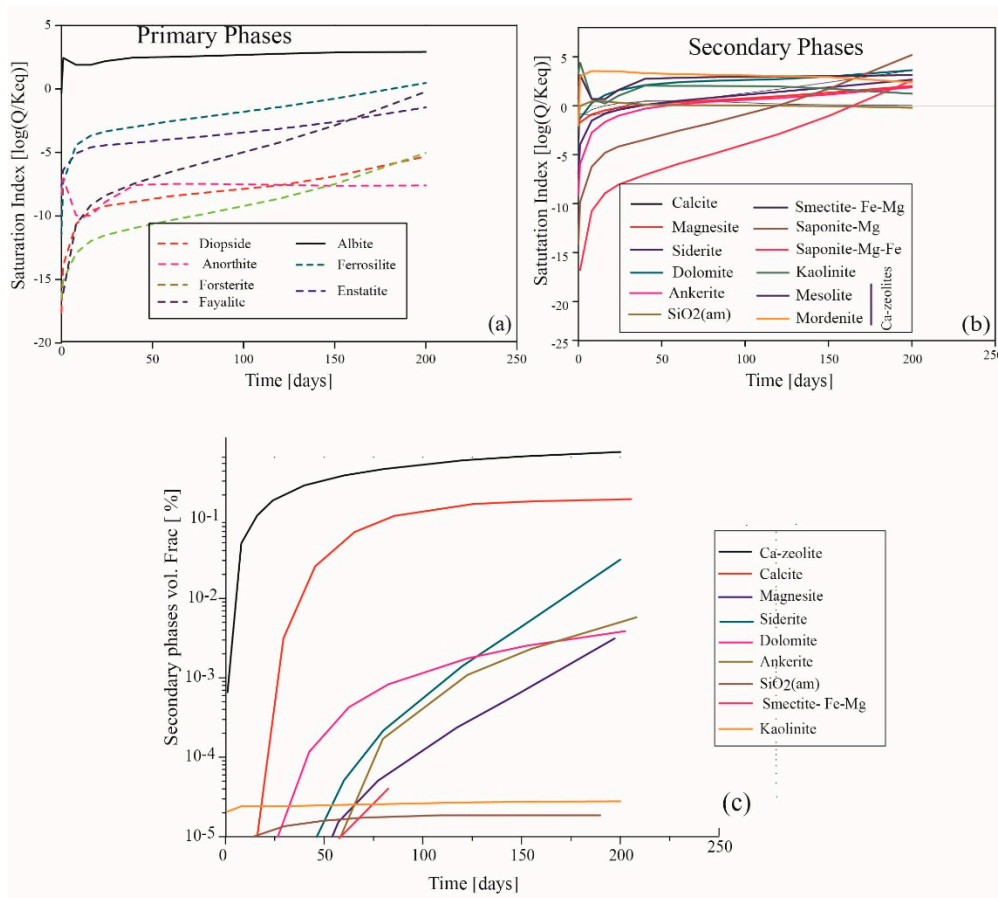
Figure 9. Evolution of the simulated saturation index: for the primary (**a**) and secondary minerals (**b**) and the variation of minerals' volume fraction (in m^3 mineral/m^3 rock) vs. time (**c**).

Table 8. Simulated dissolution and precipitation rate at t = 200 days (simulation with specific surface areas (SSA) = 120 $cm^2 \cdot g^{-1}$).

Primary Minerals	Reaction Rate ($mol \cdot L^{-1} \cdot s^{-1}$)	Secondary Minerals	Reaction Rate ($mol \cdot L^{-1} \cdot s^{-1}$)
Albite	2.77×10^{-11}	Siderite	4.13×10^{-9}
Anorthite	-1.08×10^{-9}	Calcite	5.01×10^{-10}
Fayalite	-1.24×10^{-10}	Magnesite	4.01×10^{-10}
Forsterite	-1.64×10^{-10}	Ca_zeolites	2.41×10^{-10}
Enstatite	-1.73×10^{-10}	Ankerite	8.58×10^{-11}
Diopside	-6.48×10^{-11}	Dolomite	4.84×10^{-11}
Ferrosilite	-2.57×10^{-14}	Smectite	1.31×10^{-12}
		Kaolinite	5.37×10^{-15}
		SiO$_2$	2.14×10^{-16}

Two mineral assemblages resulting from the CG alteration are predicted by the geochemical model. A Ca and Fe-Mg carbonate assemblage and another composed of Ca-Mg-Fe silicates (and aluminum) such as calcium-rich zeolites, clay minerals and amorphous silica. Ca-zeolites (mesotile and mordenite) and kaolinite are the first secondary minerals to form simultaneously with albite volume increase, followed by the amorphous silica (Figure 9c). The Si-Al-rich assemblage formation results in a sudden decrease in aluminum and silicon from the outlet solution. The carbonates' mineral phases correspond to calcite, dolomite, magnesite, siderite and ankerite. Calcite and dolomite appear in the simulations after 16 days, followed by siderite and magnesite (after 40 days). Ankerite was the last carbonate phase to precipitate, concomitant with Fe-Mg-smectite.

5. Discussion

5.1. Experimental Results

The petrographic study of the two samples, with SEM-EDS, did not reveal any carbonate phase precipitation. However, an increase in textural roughness in the samples was detected with the number of days of exposure into brine SC CO_2, as also mentioned in [61]. The diffractograms on global powdered fractions for the two experimental specimens are not considerably different between 0 and 64 days. Nevertheless, they reflect trace amounts of talc and vermiculite, as alteration products, after most experimental runs of mafic silicates. Also present is halite. The grazing incidence diffraction of CG and GD specimens, which helps to detect the mineralogy overlaid on the face specimens, additionally indicated the presence of gypsum and smectite (Table 9). Considering that talc and vermiculite were not detected by this technique within 64 days, those mineral phases should already be present before the experiments, resulting from the replacement of iron-magnesium igneous phases. Their trace amounts may justify the fact that they are not systematically detected in powder XRD. The absence of significant differences in the global mineralogical and chemical compositions of samples from the two experiments allows us to conclude that the reactions between minerals and fluids were not significant. On the other hand, the mineralogical and physical changes are limited to external areas of the CG and GD specimens exposed to CO_2-rich brine. The changes could be due to local precipitations/dissolutions at the specimen surface and could represent the early effects of influence of the CO_2-rich brine on the rock.

Table 9. Comparative summary of modelled and experimental mineral phases from cumulate gabbro (GXRD: grazing incidence geometry XRD; phases expressed as vol %).

	0 days	1 Day	4 Days	16 Days	64 Days
	Primary Phases	**Secondary Phases**			
Modelling	Clinopyroxene (52) Orthopyroxene (1.2) Olivine (10) Plagioclase (11)	Kaolinite (2.07×10^{-5}) Ca-zeolites (2.82×10^{-3})	SiO_2 am. (2.13×10^{-6}) Kaolinite (2.4×10^{-5}) Ca-zeolites (4.16×10^{-3})	Calcite (4.8×10^{-5}) Dolomite (5.28×10^{-6}) SiO_2 am (5.92×10^{-6}) Kaolinite (2.42×10^{-5}) Ca-zeolites (4.36×10^{-3})	Smectite (2.13×10^{-6}) Calcite (8.85×10^{-2}) Dolomite (8.32×10^{-4}) Magnesite (5.92×10^{-5}) Siderite (2.17×10^{-4}) Ankerite (3.95×10^{-4}) Ca-zeolites (5.54×10^{-2}) SiO_2 am. (1.31×10^{-5}) Kaolinite (2.75×10^{-5})
Experimental	Clinopyroxene (45–55) Olivine (15–20) Amphibole (10–15) Plagioclase (5–10) Ilmenite (5)	Gypsum (SEM-EDS) Halite (XRD + SEM-EDS)	Gypsum (SEM-EDS) Halite (SEM-EDS)	Gypsum (SEM-EDS) Halite (SEM-EDS)	Smectite (GXRD) Gypsum (GXRD + SEM-EDS) Halite (GXRD + SEM-EDS)

The measure of pH values in the brine is conditioned by the release of CO_2 during depressurization after chamber opening, and thus the acidity during the experiments should be even lower than that measured when the chamber is decompressed (Tables 6 and 7). However, the increase in pH correlates positively with the time of rock-brine interaction (Tables 6 and 7). The trends of the pH measurements correspond to those found in previous experimental works carried out in an autoclave [25,37–39].

The variability of the concentration of elements in the brine (Tables 6 and 7) reflects the reaction dynamics imposed by the composition of the high-salinity brine, the rock composition (Table 5) and the experimental conditions. In general, the concentrations of the experimental solutions, with higher Na and lower Ca and Mg concentrations for GD, agree with the less mafic composition of this lithotype when compared to the CG. The correlation of the measurements of Ca^{2+}, Mg^{2+} and total Fe in the brine and CaO, MgO and Fe_2O_3 in the rock is as follows:

- In the case of CG, the Ca^{2+} concentration measured in the brine shows a decrease after each run. This decrease in Ca^{2+} is not described elsewhere [14,25]. On the contrary, and in line with the

behavior of Mg^{2+} and total Fe, what is generally described is an increase in its concentration. This was also observed with the GD experiments.

- The Ca^{2+} (aqueous) decrease can be explained by the high content of this ion in the initial brine. Under the experimental conditions, Ca^{2+} should be consumed when forming secondary minerals (Ca-Al-Si; calcium aluminum silicates), as predicted by the modelling. The hypothesis that precipitation of gypsum within the autoclave could account for the Ca^{2+} decrease should be discarded, since the sulphate ion concentration is not sufficiently high. Modelling results indicate that for gypsum to precipitate the sulphate concentration should be at least double.

- The 0.4 wt. % increase in CaO in the total rock composition after a 64-day run seems to reflect not only its incorporation in the structure of Al-silicates but also the crystallization of gypsum during the drying process, after concluding the run.

- Increases of iron and magnesium in solution are in accordance with the decrease, albeit reduced, of these elements (0.4 wt. % FeO and 0.1 wt. % MgO) in the whole rock composition after 64 days. These observations are also in agreement with the textural observations, where the Fe-Mg mineral phases are the first to react with acidified brine, releasing these components into the solution.

Regarding the experiment with GD, the variation of Ca^{2+} and Mg^{2+} concentrations in brine shows a very small increase, or a tendency to remain constant. The increase is in line with what is described in the literature [25]. Such an increase in solution is reflected in the decreasing concentrations of CaO (0.42 wt. %) and MgO (0.21 wt. %) in total rock for the 64-day run specimens. FeO shows a similar trend, decreasing by 0.3 wt. % in the same specimens.

5.2. Numerical Simulation and Correlation with Experimental Results

Observations on fluid chemistry and pH changes over time indicate that, under similar conditions of P_{CO_2} and temperature, the simulation with SSA = 120 cm^2/g shows a relative agreement with the experimental data (Figures 7 and 8). The considered SSA is in the range of the specific area of olivine, plagioclase and pyroxene used in [53]. The predicted mobility of calcium is higher than for other components, with a slight increase in concentration for the first 24 days, before being incorporated within the secondary phases. As mentioned above, this increase is not reflected in Experiment 1.

The model also shows that Ca^{2+} has been consumed in Ca-zeolites and/or carbonates; for instance, mesolite and mordenite are the first phases to consume calcium at a low pH < 5.5. Moreover, the gradual increase in Mg concentration is justified by the progressive dissolution of diopside and forsterite, accompanied by a moderate precipitation of dolomite and later of magnesite. The results of the newly formed mineralogy (Table 9) indicate the presence of early neoformation phases (e.g., smectite) that can capture calcium within its structure. Nevertheless, no carbonates were observed or detected during the experiment. In CG specimens, most likely, the secondary phases might be local and covered by the considerable amount of salts lining the rock surface.

The simulation also indicates that the $\Delta(Mg/Si)$ and $\Delta(Ca/Si)$ ratios are 1.45 and 0.35, respectively, and suggests that olivine, diopside and Ca-plagioclase (the main CG minerals) dissolve stoichiometrically [25]. Therefore, the high ratio between silicon in the simulation and the experiment (Si/Si* = 10) testify to the nonstoichiometric dissolution of CG in the experiment. Furthermore, $(\Delta(Mg^*/Si^*) = 4)$ is significantly higher and denotes that magnesium dissolves faster than silica (incongruent dissolution). At pH > 5.5, Ca-Mg carbonates (namely, calcite and dolomite) start precipitating and continue up to a neutral/alkaline pH, consistent with the observations from other authors [25,55]. Calcite remains the dominant carbonate phase at a high pH, indicating its stability under alkaline conditions. Iron displayed a similar trend to Mg^{2+}, showing a high release rate. Consequently, a tiny fraction of siderite and Fe-Mg-rich smectite was precipitated, concomitant with the dissolution of the primary Fe-rich minerals (fayalite) and followed by ankerite (Ca (Fe, Mg) (CO$_3$)$_2$). The calculated silica and iron concentrations are significantly higher compared to Experiment 1.

Besides the incongruent dissolution observed in the experiments, CG rocks are less reactive than basaltic rocks. As a matter of comparison, Gysi and Stefánsson [25] measured elevated P_{CO_2},

ion and Si values in glass basalts, in the same range of the simulations (2 mmol/kgw). Note that the brine used in Experiment 1 has a CO_2 concentration 1.5 times higher than that used previously by Gysi and Stefánsson [55], and thus, according to the those authors' results, further secondary phases are expected, since dissolved CO_2 is available during the time of the experiment. The limitation in secondary phases (in CG) is due to the rock reactivity. The experiment's duration is another factor influencing the secondary phases' precipitation.

The total volume of secondary minerals predicted is 0.8 vol %, dominated mostly by zeolites (0.61% in rock volume), carbonates, especially calcite (0.172% in rock volume), and insignificant amount of clays. The small amounts of secondary phases render their identification in SEM very difficult, as reported in previous studies [62]. After 50 days, the $\Delta(Ca) < 0$ corresponds to a stage where zeolites and carbonates competed with a dominant volume of Ca-zeolites. The Mg/Si and Fe/Si ratios increased over time, resulting from the continuous dissolution of clinopyroxene and olivine and precipitating trace amounts of Mg-Fe-rich carbonates, as well as clay minerals.

SEM and XRD observations showed a significant amount of salt crystals lining the samples' surfaces. However, small amounts of Na_2O were measured in the rock, contrasting with the noticeable quantity of crystals observed in SEM images. The Na and Cl concentrations also showed a cyclic decrease and increase in concentration, not consistent with an unlikely continuous evaporation of the brine during the experiments. We believe that halite and gypsum crystallized after opening the chamber and degassing, or during drying.

As discussed in Section 2, other authors with similar experimental approaches have observed mineral carbonation occurring in time frames comparable to those applied in our experiments. Still, the lack of noticeable precipitation of carbonate minerals during our experiments was not unexpected, since the experiment was designed to look at early-phase dissolution conditions. The proportion of SC CO_2/brine/rock, was defined to ensure that the brine would always be supersaturated CO_2 during the experiments, as is expected in early-phase injections when dissolution is the dominant process. Such proportions imply that, during the whole duration of the experiments, the pH remained very low in the autoclave, and carbonates could not precipitate. Exposure of the samples to the CO_2-supersaturated brine for longer periods would probably result in consumption of the CO_2, pH increase and precipitation of carbonate minerals. Given the time constraints of the project, for the second run of experiments, with the gabbro-diorite sample, the duration of the runs was kept constant, but the CO_2/brine/rock proportion was changed. The volume of CO_2 was decreased and the mass of rock increased, to see if mineral carbonation would be observed during at least the 64-day runs. The results of this second round of experiments have not yet been fully explored as geochemical modelling is still being done, but they will be the basis for defining the physical conditions and duration of the next set of experiments.

6. Conclusions

The results obtained reveal, in the first analysis, the complexity of the systems considered: not only the mineralogy observed in the CG and GD but also the composition of the highly saline brine used in the experiments. Thus, a full fit between modelling and experimental results was not always verified.

The preliminary results of the numerical modelling indicate that carbonate precipitation is possible in a batch reactor at a low temperature and pressure (40 °C and 80 kbar). However, the amount of carbonated minerals is very small. In all the tests conducted, Ca-Mg-Fe types of carbonates (calcite, dolomite, magnesite, siderite and ankerite) are predicted, mostly after 64 days (about 0.18% in volume). At this time, carbonates are coupled with the secondary silicates (0.62 vol %) namely zeolites, clays and amorphous silica. Zeolites and amorphous silica were the first predicted phases, forming just after two days.

After 64 days, the experimental data are in line with the modelling as far as the Ca-Al-Si mineral phases. The presence of smectite was verified by grazing XRD. However, calcite, or any other carbonate also predicted by the model in small quantities, was not recorded by any of the analysis

techniques (SEM-EDS, XRD, FTIR). Both experiments detected a large amount of salt (gypsum and halite) lining on specimens' surfaces that was not reproduced by the model. Those should have precipitated after opening the chamber/during drying. Some vestigial secondary phases not detected by XRD can be hidden under the salts and not observed by SEM-EDS.

Experiment 2 with GD was not modelled, but the experimental results are in line with the observations from Experiment 1: textural features, given enhanced dissolution of ferromagnesian minerals and increased roughness with run time, and secondary mineralogy precipitation (smectite, halite and gypsum).

The measured complex variations in brine composition and total rock compositions reflect the dissolution under SC CO_2 conditions but also the contribution of the high-salinity brine.

The sensitive analysis conducted on the reactive surface area demonstrated that, for the cumulate gabbros, a specific surface area of 120 cm^2/g is required to fit the geochemical model instead of the 250 cm^2/g reported for basalt glass. Alternatively, the BET method can be applied. This preliminary model's results will provide interesting benchmarking, and other alternatives are being considered to adequately match the laboratory results.

The experimental and modelling results for 64 days essentially reflect a dissolution mechanism. For higher pH values, and for 64-day runs, the prevailing mechanism changes and significant carbonation occurs. Although in small amounts, the carbonate precipitation would be significant if upscaled to a reservoir scale. Subsequent experiments within the INCARBON project will attempt to replicate the conditions under which mineral precipitation will be the prevailing process, in order to establish a clear picture of the mineral carbonation potential in the target rocks.

References

1. IEA. *Energy Technology Perspectives 2017: Catalysing Energy Technology Transformations*; IEA/OECD, Ed.; IEA: Paris, France, 2017; p. 443. [CrossRef]
2. Bachu, S. Sequestration of CO_2 in geological media: Criteria and approach for site selection in response to climate change. *Energy Convers. Manag.* **2000**, *41*, 953–970. [CrossRef]
3. Benson, S.M.; Cole, D.R. CO_2 Sequestration in Deep Sedimentary Formations. *Elements* **2008**, *4*, 325–331. [CrossRef]
4. Sayegh, S.; Krause, F.; Girard, M.; DeBree, C. Rock/Fluid Interactions of Carbonated Brines in a Sandstone Reservoir: Pembina Cardium, Alberta, Canada. *SPE Form. Eval.* **1990**, *5*, 399–405. [CrossRef]

5.   Izgec, O.; Demiral, B.; Bertin, H.; Akin, S. CO_2 injection into saline carbonate aquifer formations I: Laboratory investigation. *Transp. Porous Media* **2008**, *72*, 1–24. [CrossRef]

6.   Gaus, I. Role and impact of CO_2-rock interactions during CO_2 storage in sedimentary rocks. *Int. J. Greenh. Gas Control* **2010**, *4*, 73–89. [CrossRef]

7.   Saeedi, A.; Rezaee, R.; Evans, B.; Clennell, B. Multiphase flow behaviour during CO_2 geo-sequestration: Emphasis on the effect of cyclic CO_2–brine flooding. *J. Pet. Sci. Eng.* **2011**, *79*, 65–85. [CrossRef]

8.   Klein, F.; McCollom, T. From serpentinization to carbonation: New insights from a CO_2 injection experiment. *Earth Planet. Sci. Lett.* **2013**, *379*, 137–145. [CrossRef]

9.   Druckenmiller, M.L.; Maroto-Valer, M.M. Carbon sequestration using brine of adjusted pH to form mineral carbonates. *Fuel Process. Technol.* **2005**, *86*, 1599–1614. [CrossRef]

10.   McGrail, B.P.; Spane, F.A.; Amonette, J.E.; Thompson, C.R.; Brown, C.F. Injection and Monitoring at the Wallula Basalt Pilot Project. *Energy Procedia* **2014**, *63*, 2939–2948. [CrossRef]

11.   Pedro, J.; Araújo, A.A.; Moita, P.; Beltrame, M.; Lopes, L.; Chambel, A.; Berrezueta, E.; Carneiro, J. Mineral carbonation of CO_2 in Mafic Plutonic Rocks, I – Screening criteria and application to a case study in SW Portugal. *Appl. Sci.* **2020**, *10*, 4879. [CrossRef]

12.   Rosenbauer, R.; Koksalan, T.; Palandri, J. Experimental investigation of CO_2-brine-rock interactions at elevated temperature and pressure: Implications for CO_2 sequestration in deep-saline aquifers. *Fuel Process. Technol.* **2005**, *86*, 1581–1597. [CrossRef]

13.   Liu, Q.; Maroto-Valer, M. Investigation of the pH effect of a typical host rock and buffer solution on CO2 sequestration in synthetic brines. *Fuel Process. Technol.* **2010**, *91*, 1321–1329. [CrossRef]

14.   Andreani, M.; Luquot, L.; Gouze, P.; Godard, M.; Hoisé, E.; Gibert, B. Experimental Study of Carbon Sequestration Reactions Controlled by the Percolation of CO_2-Rich Brine through Peridotites. *Environ. Sci. Technol.* **2009**, *43*, 1226–1231. [CrossRef]

15.   Romão, I.S.; Gando-Ferreira, L.M.; da Silva, M.M.V.G.; Zevenhoven, R. CO_2 sequestration with serpentinite and metaperidotite from Northeast Portugal. *Miner. Eng.* **2016**, *94*, 104–114. [CrossRef]

16.   Duan, Z.; Sun, R. An improved model calculating CO_2 solubility in pure water and aqueous NaCl solutions from 273 to 533 K and from 0 to 2000 bar. *Chem. Geol.* **2003**, *193*, 257–271. [CrossRef]

17.   Chizmeshya, A.V.G.; McKelvy, M.J.; Squires, K.; Carpenter, R.W.; Bearat, H. *A Novel Approach to Mineral Carbonation: Enhancing Carbonation While Avoiding Mineral Pretreatment Process Cost*; Arizona State Univ: Tempe, AZ, USA, 2007. [CrossRef]

18.   Daval, D.; Martinez, I.; Corvisier, J.; Findling, N.; Goffé, B.; Guyot, F. Carbonation of Ca-bearing silicates, the case of wollastonite: Experimental investigations and kinetic modeling. *Chem. Geol.* **2009**, *265*, 63–78. [CrossRef]

19.   Daval, D.; Sissmann, O.; Menguy, N.; Saldi, G.D.; Guyot, F.; Martinez, I.; Corvisier, J.; Garcia, B.; Machouk, I.; Knauss, K.G.; et al. Influence of amorphous silica layer formation on the dissolution rate of olivine at 90 °C and elevated pCO_2. *Chem. Geol.* **2011**, *284*, 193–209. [CrossRef]

20.   Sissmann, O.; Daval, D.; Brunet, F.; Guyot, F.; Verlaguet, A.; Pinquier, Y.; Findling, N.; Martinez, I. The deleterious effect of secondary phases on olivine carbonation yield: Insight from time-resolved aqueous-fluid sampling and FIB-TEM characterization. *Chem. Geol.* **2013**, *357*, 186–202. [CrossRef]

21.   O.´Connor, W.; Dahlin, D.; Nilsen, D.; Rush, G.E.; Walters, R.; Turner, P. Carbon Dioxide Sequestration by Direct Mineral Carbonation: Results from Recent Studies and Current Status. In Proceedings of the First National Conference on Carbon Sequestration, Washington, DC, USA, 14–17 May 2001.

22.   Béarat, H.; McKelvy, M.J.; Chizmeshya, A.V.G.; Gormley, D.; Nunez, R.; Carpenter, R.W.; Squires, K.; Wolf, G.H. Carbon Sequestration via Aqueous Olivine Mineral Carbonation: Role of Passivating Layer Formation. *Environ. Sci. Technol.* **2006**, *40*, 4802–4808. [CrossRef]

23.   Gerdemann, S.J.; O'Connor, W.K.; Dahlin, D.C.; Penner, L.R.; Rush, H. Ex Situ Aqueous Mineral Carbonation. *Environ. Sci. Technol.* **2007**, *41*, 2587–2593. [CrossRef]

24.   Soong, Y.; Fauth, D.L.; Howard, B.H.; Jones, J.R.; Harrison, D.K.; Goodman, A.L.; Gray, M.L.; Frommell, E.A. CO_2 sequestration with brine solution and fly ashes. *Energy Convers. Manag.* **2006**, *47*, 1676–1685. [CrossRef]

25.   Gysi, A.P.; Stefánsson, A. CO_2-water-basalt interaction. Low temperature experiments and implications for CO_2 sequestration into basalts. *Geochim. Cosmochim. Acta* **2012**, *81*, 129–152. [CrossRef]

26. Alfredsson, H.A.; Oelkers, E.H.; Hardarsson, B.S.; Franzson, H.; Gunnlaugsson, E.; Gislason, S.R. The geology and water chemistry of the Hellisheidi, SW-Iceland carbon storage site. *Int. J. Greenh. Gas Control* **2013**, *12*, 399–418. [CrossRef]

27. Matter, J.M.; Stute, M.; Snaebjornsdottir, S.O.; Oelkers, E.H.; Gislason, S.R.; Aradottir, E.S.; Sigfusson, B.; Gunnarsson, I.; Sigurdardottir, H.; Gunnlaugsson, E.; et al. Rapid carbon mineralization for permanent disposal of anthropogenic carbon dioxide emissions. *Science* **2016**, *352*, 1312–1314. [CrossRef]

28. Kaszuba, J.; Janecky, D.; Snow, M. Carbon dioxide reaction processes in a model brine aquifer at 200°C and 200 bars: Implications for geologic sequestration of carbon. *Appl. Geochem.* **2003**, *18*, 1065–1080. [CrossRef]

29. Peuble, S.; Godard, M.; Luquot, L.; Andreani, M.; Martinez, I.; Gouze, P. CO_2 geological storage in olivine rich basaltic aquifers: New insights from reactive-percolation experiments. *Appl. Geochem.* **2015**, *52*, 174–190. [CrossRef]

30. Peuble, S.; Godard, M.; Gouze, P.; Leprovost, R.; Martinez, I.; Shilobreeva, S. Control of CO_2 on flow and reaction paths in olivine-dominated basements: An experimental study. *Geochim. Cosmochim. Acta* **2019**, *252*, 16–38. [CrossRef]

31. McGrail, B.P.; Schaef, H.T.; Ho, A.M.; Chien, Y.J.; Dooley, J.J.; Davidson, C.L. Potential for carbon dioxide sequestration in flood basalts. *J. Geophys. Res. Solid Earth* **2006**, *111*, B12. [CrossRef]

32. Schaef, H.T.; McGrail, B.P. Dissolution of Columbia River Basalt under mildly acidic conditions as a function of temperature: Experimental results relevant to the geological sequestration of carbon dioxide. *Appl. Geochem.* **2009**, *24*, 980–987. [CrossRef]

33. Kanakiya, S.; Adam, L.; Esteban, L.; Rowe, M.C.; Shane, P. Dissolution and secondary mineral precipitation in basalts due to reactions with carbonic acid. *J. Geophys. Res. Solid Earth* **2017**, *122*, 4312–4327. [CrossRef]

34. André, L.; Audigane, P.; Azaroual, M.; Menjoz, A. Numerical modeling of fluid–rock chemical interactions at the supercritical CO_2–liquid interface during CO_2 injection into a carbonate reservoir, the Dogger aquifer (Paris Basin, France). *Energy Convers. Manag.* **2007**, *48*, 1782–1797. [CrossRef]

35. Gaus, I.; Audigane, P.; Andre, L.; Lions, J.; Jacquemet, N.; Dutst, P.; Czernichowski-Lauriol, I.; Azaroual, M. Geochemical and solute transport modelling for CO_2 storage, what to expect from it? *Int. J. Greenh. Gas Control* **2008**, *2*, 605–625. [CrossRef]

36. Berrezueta, E.; González-Menéndez, L.; Breitner, D.; Luquot, L. Pore system changes during experimental CO_2 injection into detritic rocks: Studies of potential storage rocks from some sedimentary basins of Spain. *Int. J. Greenh. Gas Control* **2013**, *17*, 411–422. [CrossRef]

37. Luquot, L.; Gouze, P. Experimental determination of porosity and permeability changes induced by injection of CO_2 into carbonate rocks. *Chem. Geol.* **2009**, *265*, 148–159. [CrossRef]

38. Tarkowski, R.; Wdowin, M.; Manecki, M. Petrophysical examination of CO_2-brine-rock interactions—results of the first stage of long-term experiments in the potential Zaosie Anticline reservoir (central Poland) for CO_2 storage. *Environ. Monit. Assess.* **2014**, *187*, 4215. [CrossRef]

39. Berrezueta, E.; Ordoñez Casado, B.; Quintana, L. Qualitative and quantitative changes in detrital reservoir rocks caused by CO_2 – brine – rock interactions during first injection phases (Utrillas sandstones, northern Spain). *Solid Earth* **2016**, *7*, 37–53. [CrossRef]

40. Lake, L.W. *Enhanced Oil Recovery*; Prentice Hall: Englewood Cliffs, NJ, USA, 1989.

41. Span, R.; Wagner, W. A New Equation of State for Carbon Dioxide Covering the Fluid Region from the Triple-Point Temperature to 1100 K at Pressures up to 800 MPa. *J. Phys. Chem. Ref. Data* **1996**, *25*, 1509–1596. [CrossRef]

42. Holloway, S. An overview of the underground disposal of carbon dioxide. *Energy Convers. Manag.* **1997**, *38*, S193–S198. [CrossRef]

43. Georgiou, C.D.; Sun, H.J.; McKay, C.P.; Grintzalis, K.; Papapostolou, I.; Zisimopoulos, D.; Panagiotidis, K.; Zhang, G.; Koutsopoulou, E.; Christidis, G.E.; et al. Evidence for photochemical production of reactive oxygen species in desert soils. *Nat. Commun.* **2015**, *6*, 7100. [CrossRef]

44. Beltrame, M.; Liberato, M.; Mirão, J.; Santos, H.; Barrulas, P.; Branco, F.; Gonçalves, L.; Candeias, A.; Schiavon, N. Islamic and post Islamic ceramics from the town of Santarém (Portugal): The continuity of ceramic technology in a transforming society. *J. Archaeol. Sci. Rep.* **2019**, *23*, 910–928. [CrossRef]

45. Steefel, C.; Lasaga, A. A Coupled Model for Transport of Multiple Chemical-Species and Kinetic Precipitation Dissolution Reactions with Application to Reactive Flow in Single-Phase Hydrothermal Systems. *Am. J. Sci.* **1994**, *294*, 529–592. [CrossRef]

46. Steefel, C.I. *CrunchFlow Software for Modeling Multicomponent Reactive Flow and Transport*; User's Manual; Earth Sciences Division, Lawrence Berkeley, National Laboratory: Berkeley, CA, USA, 2009; pp. 12–91.

47. Steefel, C.; Appelo, T.; Arora, B.; Jacques, D.; Kalbacher, T.; Kolditz, O.; Lagneau, V.; Lichtner, P.; Mayer, K.; Meeussen, J.; et al. Reactive transport codes for subsurface environmental simulation. *Comput. Geosci* **2014**, 19. [CrossRef]

48. Lasaga, A.C. Rate laws of chemical reactions. In *kinetics of geochemical processes*; Lasaga, A., Kirkpatrick, R., Eds.; Mineralogical Society of America: Washington DC, USA, 1981; Volume 8, pp. 1–68.

49. Lasaga, A. Chemical Kinetics of Water-Rock Interaction. *J. Geophys. Res.* **1984**, *89*, 4009–4025. [CrossRef]

50. Aagaard, P.; Helgeson, H.C. Thermodynamic and kinetic constraints on reaction rates among minerals and aqueous solutions; I, Theoretical considerations. *Am. J. Sci.* **1982**, *282*, 237–285. [CrossRef]

51. Canilho, M.H. *Elementos de geoquímica do maciço ígneo de Sines*; Ciências da Terra UNL: Caparica, Portugal, 1989; pp. 65–80.

52. Palandri, J.; Kharaka, Y. *A Compilation of Rate Parameters of Water-Mineral. Interaction Kinetics for Application to Geochemical Modeling*; Geological Survey: Reston, VA, USA, 2004; p. 71.

53. Xu, T.; Apps, J.A.; Pruess, K. Numerical simulation of CO_2 disposal by mineral trapping in deep aquifers. *Appl. Geochem.* **2004**, *19*, 917–936. [CrossRef]

54. Geloni, C.; Giorgis, T.; Battistelli, A. Modeling of Rocks and Cement Alteration due to CO_2 Injection in an Exploited Gas Reservoir. *Transp. Porous Media* **2011**, *90*, 183–200. [CrossRef]

55. Gysi, A.P.; Stefánsson, A. CO_2–water–basalt interaction. Numerical simulation of low temperature CO_2 sequestration into basalts. *Geochim. Cosmochim. Acta* **2011**, *75*, 4728–4751. [CrossRef]

56. Geloni, C.; Giorgis, T.; Biagi, S.; Previde Massara, E.; Battistelli, A. Modeling of Well Bore Cement Alteration as a Consequence of CO_2 Injection in an Exploited Gas Reservoir. In Proceedings of the 5th Meeting of the Wellbore Integrity Network, Calgary, AB, Canada, 12–13 May 2009.

57. Koenen, M.; Wasch, L. Reactive Surface Area in Geochemical Models-Lessons Learned from a Natural Analogue. In Proceedings of the Second EAGE Sustainable Earth Sciences (SES) Conference and Exhibition, Pau, France, 30 September–4 October 2013.

58. Wolery, T.J.; Jackson, K.J.; Bourcier, W.L.; Bruton, C.J.; Viani, B.E.; Knauss, K.G.; Delany, J.M. Current Status of the EQ3/6 Software Package for Geochemical Modeling. In *Chemical Modeling of Aqueous Systems II*; American Chemical Society: Washington, DC, USA, 1990; Volume 416, pp. 104–116.

59. Helgeson, H.C.; Garrels, R.M.; MacKenzie, F.T. Evaluation of irreversible reactions in geochemical processes involving minerals and aqueous solutions—II. Applications. *Geochim. Cosmochim. Acta* **1969**, *33*, 455–481. [CrossRef]

60. Moita, P.; Berrezueta, E.; Pedro, J.; Miguel, C.; Beltrame, M.; Galacho, C.; Mirão, J.; Araújo, A.; Lopes, L.; Carneiro, J. Experiments on mineral carbonation of CO_2 in gabbro's from the Sines massif-first results from project InCarbon. *Comunicações Geológicas* **2020**, *107*, 91–96.

61. Wells, R.K.; Xiong, W.; Giammar, D.; Skemer, P. Dissolution and surface roughening of Columbia River flood basalt at geologic carbon sequestration conditions. *Chem. Geol.* **2017**, *467*, 100–109. [CrossRef]

62. Dávila, G.; Luquot, L.; Soler, J.M.; Cama, J. 2D reactive transport modeling of the interaction between a marl and a CO_2-rich sulfate solution under supercritical CO_2 conditions. *Int. J. Greenh. Gas Control* **2016**, *54*, 145–159. [CrossRef]